

# Ionic liquid functionalized tin halide perovskite investigated by STXM and spectro-ptychography

Tianxiao Sun <sup>a,\*,#</sup>, Shengnan Zuo <sup>a,#</sup>, Bo He <sup>b,c</sup>, Xinye Yuan <sup>b,c</sup>, Guixiang Li <sup>a</sup>, Jigang Zhou <sup>d</sup>, Markus Weigand <sup>a</sup>, Antonio Abate <sup>a,\*</sup>, Jian Wang <sup>d,\*</sup>

<sup>a</sup> Helmholtz-Zentrum Berlin für Materialien und Energie GmbH, Albert-Einstein-Straße 15, 12489 Berlin, Germany

<sup>b</sup> School of Physical Science and Technology, ShanghaiTech University, Shanghai 201210, China

<sup>c</sup> Center for Transformative Science, ShanghaiTech University, Shanghai 201210, China

<sup>d</sup> Canadian Light Source Inc., University of Saskatchewan, Saskatoon, SK S7N 2V3, Canada

**\* Corresponding authors:**

Email address: tianxiao.sun@helmholtz-berlin.de; antonio.abate@helmholtz-berlin.de; jian.wang@lightsource.ca

**# These authors contributed equally to this work.**

## Abstract

The structural and compositional properties of tin halide perovskite ( $(\text{CH}(\text{NH}_2)_2\text{SnI}_3$ ,  $\text{FASnI}_3$ ) with and without 1-Ethyl-3-methylimidazolium bis(trifluoromethylsulfonyl) imide (EMITFSI) were investigated using the scanning transmission soft X-ray microscopy (STXM) and spectro-ptychography techniques at the Sn  $M_{5,4}$ -edge, I  $M_{5,4}$ -edge, O K-edge, C K-edge, and N K-edge. The study offers a comprehensive interpretation of the spectral characteristics of main components (C, N, Sn, and I) in Sn-based perovskites through STXM-based techniques and further reveals differences between the perovskite samples with and without adding EMITFSI ionic liquid. The chemical imaging of Sn and I shows that the perovskite sample without ionic liquid has Sn-rich regions in iodine cavities, while the ionic liquid-treated sample exhibits a more homogeneous perovskite phase. Furthermore, the C and N K-edge XANES resonance features support the interaction between the non-volatile ionic liquid and  $\text{FA}^+$ , thus playing a protective role in the formation and stabilization of perovskite phase.

## Introduction

Halide perovskite solar cells (PVSCs) have gained recognition as highly promising candidates for next-generation photovoltaic semiconductors, with Pb-based PVSCs

being particularly attractive due to their high efficiency and stability.<sup>1-3</sup> Most research efforts are currently focused on developing effective additives like ionic liquids to enhance their stability and efficiency.<sup>4-6</sup> Specifically, the addition of 1-Ethyl-3-methylimidazolium bis(trifluoromethylsulfonyl) imide (EMITFSI, Fig. S1) has been found to improve the film quality of perovskites, and then boost the power conversion efficiency (PCE), thermal stability, and long-term stability of PVSCs.<sup>7</sup> According to Shen et al.<sup>8</sup>, the effect observed above can be attributed to the fact that the organic long-chain cations restrict the structural freedom and stabilize the orientated structure, thereby promoting the formation of perovskite films with improved crystallinity and orientation. However, the use of Pb in these cells raises concerns about toxicity and environmental impact.<sup>9-11</sup> Thus, recent research has pivoted towards Sn-based perovskites, which have garnered attention due to their environmentally friendly nature and narrow bandgap.<sup>12,13</sup> While it is believed that EMITFSI potentially has a positive impact on Sn-based perovskites, similar to its effect on Pb-based perovskites, the application of EMITFSI to Sn-based perovskites is a relatively uncharted territory, and the absence of suitable characterization methods hinders a full understanding of its effect and mechanism. This highlights the need for further research in this area to advance our understanding of the role of EMITFSI in Sn-based perovskites and unlock their full potential for photovoltaic applications.

Scanning transmission soft X-ray microscopy (STXM) is a state-of-the-art method for investigating the structure and composition of materials at the micro and nano scales.<sup>14-16</sup> It utilizes synchrotron radiation in the soft X-ray band, which is focused by a zone plate (ZP) and passes through an order sorting aperture (OSA) to eliminate any stray and higher orders light. The beam then illuminates a sample area of tens of square micrometers and is recorded by a point detector photomultiplier tube (PMT). By performing a two-dimensional grid scan on the sample, the X-ray absorption capacity of each sample spot is mapped into a pixel in a two-dimensional image, revealing different thickness or materials within the sample.<sup>17</sup> The outstanding spatial resolution (~30 nm) and energy resolution (~10000 resolving power) of STXM make it a versatile tool with a wide range of applications across multiple fields including medicine<sup>18</sup>,

archaeology<sup>19,20</sup>, agriculture<sup>21</sup>, environment<sup>22</sup>, energy storage<sup>23</sup>, and astronomy<sup>24</sup>. Recently, advanced studies by Jun et al.<sup>25</sup> and Dindault et al.<sup>26</sup> have highlighted the benefits of using STXM for the investigation of Pb-based perovskites. Their findings have shown that STXM provides high spatial resolution, high sensitivity to elements, and low radiation damage, which make STXM a highly suitable technique for studying perovskites. Furthermore, the lensless computational imaging technique of STXM-ptychography offers an innovative approach, capturing the scattering patterns of the sample with a CCD or sCMOS area detector and reconstructing them into a real-space image through mathematical algorithms.<sup>27</sup> This technique, through iterative reconstruction, can produce both amplitude (absorption) and phase images. The contrast in the phase image is based on the sample-induced phase difference from the incident light, which is typically related to the sample's optical thickness and complex refractive index. The Kramers-Kronig relationship enables the deduction of phase and absorption from each other, thus allowing the inverted peak in the phase spectrum to aid in identifying elements with low radiation damage at the pre-edges. Moreover, the amplitude and phase images produced by ptychography can achieve sub-10 nm spatial resolution and may provide more detailed morphology and chemical characteristics of the Sn-based perovskites.

In this study, we characterized Sn-based perovskites ( $\text{CH}(\text{NH}_2)_2\text{SnI}_3$ ) without (control) and with EMITFSI treatment (PVK/EMITFSI) using a combination of STXM and spectro-ptychography techniques. The STXM measurements were conducted at the Sn  $M_{5,4}$ -edge, I  $M_{5,4}$ -edge, O K-edge, C K-edge, and N K-edge, whereas the spectro-ptychography was performed at the Sn  $M_{5,4}$ -edge to investigate the impact and mechanism of the EMITFSI ionic liquid on Sn-based perovskites. The compositional analysis of Sn and I in the perovskite samples reveals that the control film has areas that are rich in Sn, located within I cavities. After the addition of ionic liquid, it results in a more uniform distribution of Sn throughout the PVK/EMITFSI film. Furthermore, the results of the C and N K-edge XANES spectromicroscopy strongly indicate that the non-volatile ionic liquid interacts with the perovskite film, playing a crucial role in maintaining its stability. This result is a valuable contribution to the understanding of

the role of the EMITFSI ionic liquid in optimizing Sn-based perovskites. By promoting a more uniform distribution of tin within the perovskite phase, which serves as a protective layer, the addition of EMITFSI has the potential to enhance the performance and stability of Sn-based perovskites. Additionally, this study marks the debut of STXM as a characterization tool for Sn-based perovskites, demonstrating its remarkable potential for studying the structures and properties of these materials.

## **Experimental section**

### **Sample fabrication**

1 mmol FAI (Dyename, Formamidinium iodide; 99.99%) and 1 mmol SnI<sub>2</sub> (TCI, Tin (II) iodide, 99.999%) were dissolved in DMSO (Sigma Aldrich, Dimethyl sulfoxide) forming a nominal concentration of 1M, stirred in a shaker at room-temperature. For the perovskite with EMITFSI (Sigma Aldrich), EMITFSI was added at 0.5 mol% to the perovskite solution. After mixed, 100  $\mu$ L perovskite precursor solution was dripped onto an indium tin oxide (ITO) substrate which was pre-cleaned by 2% Mucosol solution (Schülke & Mayr GmbH) in deionized water, acetone, isopropanol and ethanol solvents sequentially with sonication for 15 min. The sample was spin-coated at 5000 rpm for 60s with a ramp of 1000 rpm/s, then 150  $\mu$ L Chlorobenzene (Sigma Aldrich) as anti-solvent was dripped in the film at 40 s after spin coating, followed by annealing on a hotplate at 100 °C for 10 min.

### **STXM measurement**

The Sn-based perovskite samples for STXM measurement were prepared by scraping the spin-coated perovskite film into a powder form, dispersing them in toluene, and then depositing them onto conventional 500 \* 500  $\mu$ m<sup>2</sup> STXM silicon nitride windows. All STXM measurements were carried out under a high vacuum of 10<sup>-5</sup> mbar. The STXM energy stack at the Sn M<sub>5,4</sub>-edge was measured by MYSYTIIC endstation at the UE48\_EMIL beamline of the BESSY II light source, Germany. The energy of both the control and PVK/EMITFSI samples was scanned from 485 to 507 eV with an increment of 0.301 eV and a dwell time of 1 ms. And the STXM data for C, N, O K-edges and I

M<sub>5,4</sub>-edge were obtained using the ambient STXM at the 10ID-1 SM beamline of the Canadian Light Source (CLS), Canada. The energy of two perovskite films was scanned from 280 to 320 eV at the C K-edge, 395 to 430 eV at the N K-edge, 520 to 560 eV at the O K-edge, and 615 to 720 eV at the I M<sub>5,4</sub>-edge, all with varied energy step size of 0.2 to 0.5 eV at the XANES features and coarser in the pre- and post-edges, and using 1 ms dwell time. All STXM data analysis, including alignment of stack images, O.D. conversion and PCA-CA analysis, were performed using the aXis2000 software package (Adam P. Hitchcock group, McMaster University, Canada).

### **Spectro-ptychography measurement**

The perovskite samples used for STXM-ptychography were the same silicon nitride window samples as the conventional STXM measurement. The ptychography measurement in defocus mode under a high vacuum of 10<sup>-5</sup> mbar utilized a 40 nm outer-zone-width zone plate to focus the monochromatic soft X-ray beam to the plane off the focal plane of the sample to produce a 2.5 μm beam spot on the sample. The sample was raster scanned in 8 \* 8 pixels with 0.5 μm increments, providing sufficient overlap of the scanned area. To block all but the first-order beam from the zone plate, an order-sorting aperture (OSA) of 50 μm was used. The diffraction images were captured on a Tucsen Dhyana 95V2 water-cooled sCMOS camera, with a resolution of 2048 \* 2048 pixels, which was cooled to -10 °C and positioned 130 mm downstream from the sample. Moreover, the spectro-ptychography technique was used to conduct energy stacks at the Sn M<sub>5,4</sub>-edge for two Sn-based perovskite films. The energy range of the experiments was from 482.5 to 500 eV with a step size of 0.3 eV and a dwell time of 300 ms. The ptychography results were obtained through batch reconstruction using the PyPIE software (SM beamline team, Canadian Light Source, Canada).<sup>27</sup>

## **Results and discussions**

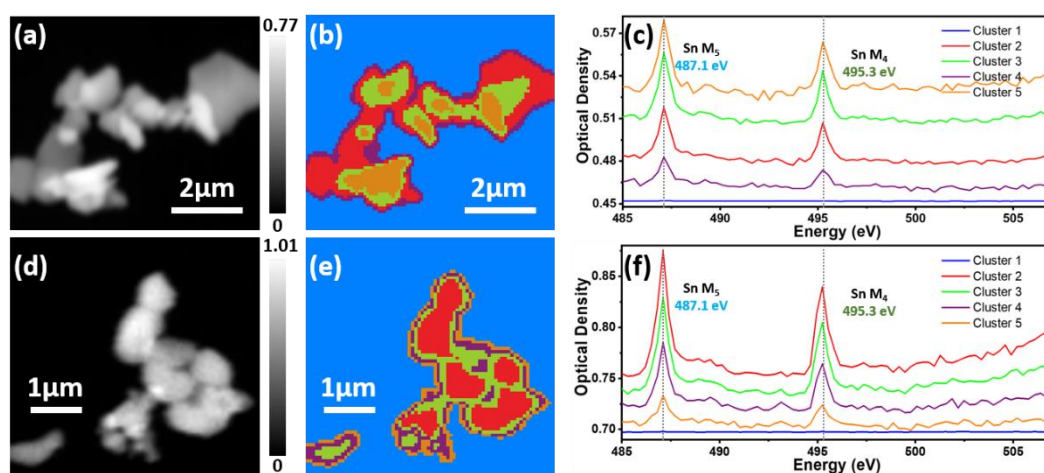


**Figure 1.** Conventional STXM results at Sn M<sub>5,4</sub>-edge of Sn-based control and PVK/EMITFSI films. (a) Averaged STXM O.D. image from Sn M<sub>5,4</sub>-edge of the control sample. (b) The PCA-CA analysis for different components of the control sample. (c) XAS spectra at Sn M<sub>5,4</sub>-edge in different regions extracted from (b). (d) Averaged STXM O.D. image from Sn M<sub>5,4</sub>-edge of the PVK/EMITFSI sample. (e) The PCA-CA analysis for different components of the PVK/EMITFSI sample. (f) XAS spectra at Sn M<sub>5,4</sub>-edge in different regions extracted from (e).

Fig. 1 shows the analysis results of the conventional STXM technique at the Sn M<sub>5,4</sub>-edge. To quantify the distribution of analyzed elements, the averaged absorption images (Fig. 1a, and d) have been converted into optical density (O.D.) maps so that the gray value of the image is directly proportional to the concentration of the elements. Fig. 1a and d showcase the morphology of the control and PVK/EMITFSI samples, respectively, which reflect the uneven distribution of tin within the sample particles based on contrast variations. The distribution of chemical phases within the samples was mapped out using the principal component analysis-cluster analysis (PCA-CA), which is depicted in Fig. 1b and e using different colors to highlight each phase/region. Fig. 1c and f display the average Sn M<sub>5,4</sub>-edge spectra extracted from the various colorful clusters shown in Fig. 1b and e, respectively, with the purpose of characterizing the chemical state and local environment of Sn within the samples. The colors used in these spectra are corresponding to those of clusters in Fig. 1b and e. All the XANES spectra at the Sn M<sub>5,4</sub> -edge, Fig. 1c and 1f, exhibit two prominent peaks at ~487.1 and ~495.3 eV. These peaks are indicative of d-shell (3d<sub>5/2</sub> and 3d<sub>3/2</sub>) to unoccupied p/f-shell electric dipole transitions, which are caused by spin-orbit splitting. These resonance

features are in agreement with the characteristic features of  $\text{Sn}^{2+}$  reported in previous literature<sup>28,29</sup>, whereas the spectrum of  $\text{Sn}^{4+}$  displays a distinct two-set triplet structure, which suggests that Sn in both control and PVK/EMITFSI films is predominantly present in a divalent state during the preparation and characterization of the perovskites. The O K-edge spectra of both samples (Fig. S2) indicated no evidence of oxygen introduced during sample preparation but the incident beam profile, suggesting that the perovskite structure remained intact and was not oxidized. Additionally, the averaged full width at half maximum (FWHM) of the absorption peaks at 487.1 eV in the control film is approximately 0.76 eV, whereas the averaged FWHM narrows to 0.60 eV in the PVK/EMITFSI film. This suggests that the excited state lifetime of the PVK/EMITFSI sample is shorter, which implies that the Sn-based perovskite with the addition of the ionic liquid exhibits more well-defined electronic states in a more homogeneous electronic environment.

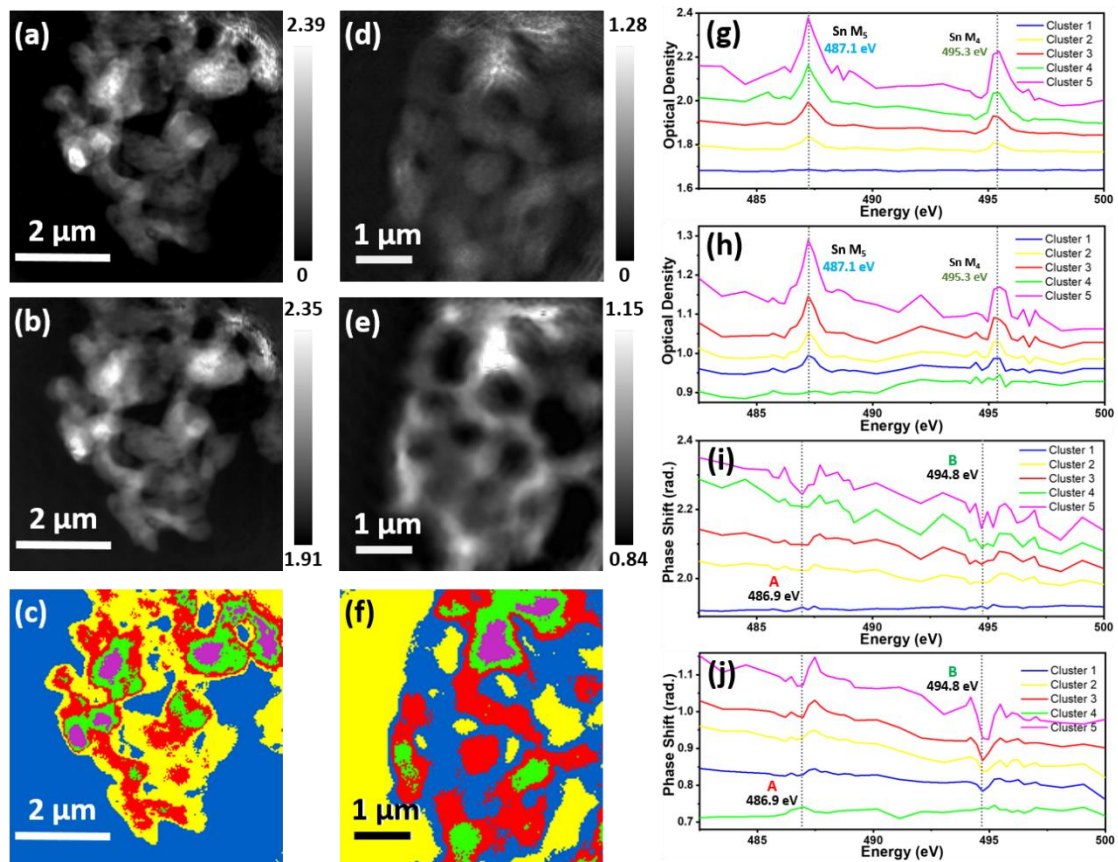


**Figure 2.** STXM spectro-ptychography results at Sn  $M_{5,4}$ -edge of Sn-based control and PVK/EMITFSI films. (a, b) Averaged ptychography amplitude image (O.D.) and phase image from

Sn  $M_{5,4}$ -edge of the control sample, respectively. (c) The PCA-CA analysis by amplitude images for different components of the control sample. (d, e) Averaged ptychography amplitude image (O.D.) and phase image from Sn  $M_{5,4}$ -edge of the PVK/EMITFSI sample, respectively. (f) The PCA-CA analysis by amplitude images for different components of the PVK/EMITFSI sample. (g, h) Absorption spectra at Sn  $M_{5,4}$ -edge in different regions extracted from (c) and (f), respectively. (i, j) Phase spectra at Sn  $M_{5,4}$ -edge in different regions extracted from (c) and (f), respectively.

Moreover, spectro-ptychography with increased spatial resolution can provide more intricate information about the morphology, by considering both the amplitude (Fig. 2a and d) and phase (Fig. 2b and e) images. The PCA-CA analysis (Fig. 2c and f) performed using the amplitude data can yield more precise clustering results compared to conventional STXM, while their average absorption spectra (Fig. 2g and h) in different regions still maintaining a high degree of consistency with the above conclusions derived from the conventional STXM analysis. Furthermore, the average phase spectra (Fig. 2i and j) of the same cluster regions of both samples were also extracted from the phase image stacks. The phase spectra at Sn  $M_{5,4}$ -edge show two inverted peaks A and B at approximately 486.9 eV and 494.8 eV, respectively. Both A and B are shifted to lower energies by roughly 0.2 eV and 0.5 eV in comparison to their corresponding absorption peaks. This resonance-structure relationship of the phase and absorption spectra is consistent with that reported in the literature by Zhu et al.<sup>30</sup>. It is worth noting that the thickness of the sample has a significant impact on the degree of phase shift observed in the phase spectra. In general, the baselines of the phase spectra are more separated from the background sample-free region compared to the absorption spectra. In addition, changes in XANES features could be more sensitive in the phase spectra. For instance, in the PVK/EMITFSI sample, the two inverted peaks of the phase spectrum changed by 67.7% and 40.6%, respectively, in the thickest region (purple region in Fig. 2f) relative to the second thickest region (red region in Fig. 2f), whereas the corresponding absorption peaks only changed by 31% and 37.5%, respectively. This implies that the phase spectrum could be more sensitive to changes in sample thickness than the absorption spectrum, which could potentially offer an advantage in studying the morphology of the Sn-based perovskite film.

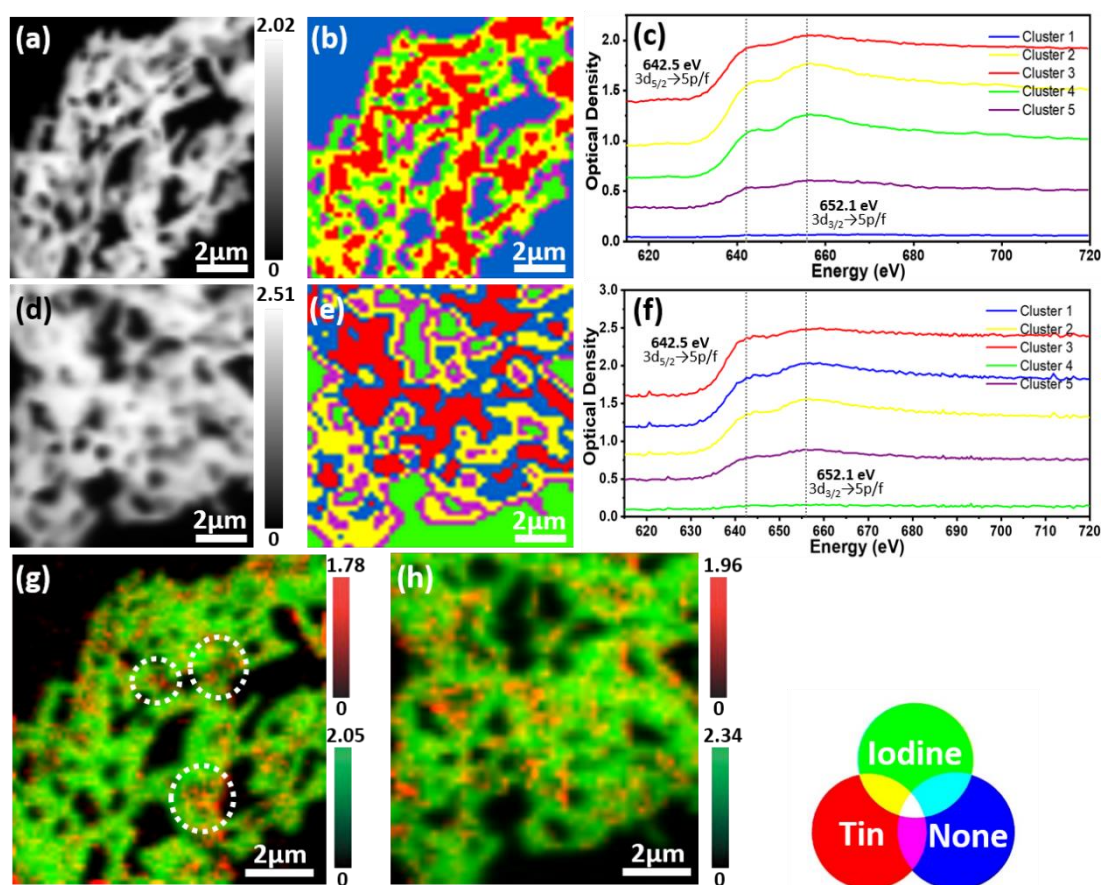


**Figure 3.** Conventional STXM results at I  $M_{5,4}$ -edge of Sn-based control and PVK/EMITFSI films. (a) Averaged STXM O.D. image from I  $M_{5,4}$ -edge of the control sample. (b) The PCA-CA analysis for different components of the control sample. (c) XAS spectra at I  $M_{5,4}$ -edge in different regions extracted from (b). (d) Averaged STXM O.D. image from I  $M_{5,4}$ -edge of the PVK/EMITFSI sample. (e) The PCA-CA analysis for different components of the PVK/EMITFSI sample. (f) XAS spectra at I  $M_{5,4}$ -edge in different regions extracted from (e). (g, h) The color composite maps for relevant components of the Sn-based control and PVK/EMITFSI samples, respectively: red represents tin and green represents iodine. The individual component maps have been rescaled in each respective color channel. The white circles in Fig. 2g highlight the regions where tin is noticeably accumulated within iodine cavities.

Such sample heterogeneity difference is also reflected in the investigation at I  $M_{5,4}$ -edge for Sn-based perovskite samples treated with and without EMITFSI (Fig. 3). Fig. 3a and d describe the morphology of the control and PVK/EMITFSI films by O.D., respectively, while the PCA-CA analysis of the two samples is presented Fig. 3b, c and Fig. 3e, f, respectively. The I  $M_{5,4}$ -edge XANES has been observed in Pb-based perovskites<sup>25,26</sup>, showing two main resonance features, which are understudied in Sn-

based perovskites. All the average spectra (Fig. 3c and f) of the different cluster regions of the two samples obtained by PCA-CA analysis present two broad absorption peaks at  $\sim 642.5$  eV and  $\sim 652.1$  eV, which are assigned to I  $3d_{5/2}$  and  $3d_{3/2}$  to 5p or 5f transition, respectively. The spectra in these samples bear similarities to the resonance structures observed in Pb-based perovskites, however, the peak positions are shifted towards lower energies by approximately 7 eV. This shift is attributed to tin being a less metallic element compared to lead, leading to lower binding energy in covalent bonds with iodine. It is noteworthy that in the control sample, the edge jumps of the average absorption spectra from the thickest to the thinnest region are 0.43, 0.55, 0.41, and 0.16 (corresponding to the red, yellow, green, and purple regions in Fig. 3b, respectively), whereas in the PVK/EMITFSI sample, they are 0.755, 0.60, 0.47, and 0.25 (corresponding to the red, blue, yellow, and purple regions in Fig. 3e, respectively). The observation shows that the spectrum of the thickest red sample region in Fig. 3c does not exhibit the highest edge jump. Conversely, Fig. 3f reveals a trend that aligns with the sample thickness and iodine concentration, although thicker red area in the PVK/EMITFSI sample may suffer from greater signal saturation suppression.

This phenomenon is more clearly depicted in the color composite images of tin and iodine. The color composite image of the control sample (Fig. 3g) displays a significant accumulation of tin in the cavities of the iodine frame, particularly in the area marked by the white circles, and this phenomenon has been improved to a certain extent in the PVK/EMITFSI sample as shown in Fig. 3h. This indicates that the addition of EMITFSI ionic liquid is beneficial in promoting the formation and stability of Sn-based perovskite films.

Furthermore, to uncover deeper insights into the interaction mechanisms of EMITFSI ionic liquid on Sn-based perovskites, we also utilized STXM to investigate the two Sn-based perovskites at the carbon and nitrogen K-edges (Fig. 4). The PCA-CA analysis of the two perovskites reveals two prominent resonance features at carbon K-edge. The first resonance peak is attributed to  $C1s \rightarrow \pi^*$  (C=N) transition at  $\sim 287.5$  eV and is in line with the only peak at  $\sim 401.3$  eV in the N K-edge absorption spectra (Fig. 4g and h). This agrees with a significant amount of C=N double bonds from formamidinium

iodide (FAI). A close observation of the carbon K-edge absorption spectra reveals that the  $C1s \rightarrow \pi^*(C=N)$  transition peak is located at approximately 287.5 eV in the control film, while the peak is shifted to higher energy of 287.9 eV in the PVB/EMITFSI film. Notably, a similar chemical shift is not observed in the nitrogen K-edge XANES results. This is probably because  $EMI^+$ , as a nucleophile, reacts more readily with carbon, which has a lower electron density compared to nitrogen, causing a slight perturbation in the carbon spectrum. Furthermore, the second peak at  $\sim 291.4$  eV in the carbon K-edge spectra probably represents the  $C1s \rightarrow \sigma^*(C-F)$  transition. There is also a slight bump at 291.4 eV in the control sample, which could be due to the contribution of dimethyl sulfoxide (DMSO) and other  $C1s \rightarrow \sigma^*$  transitions. However, for the EMITFSI-treated sample, the peak intensity increased significantly, particularly in the red area shown in Fig. 4d. This indicates the F-containing EMITFSI is not only adsorbed on the perovskite film, but also has a substantial interaction with the perovskite film.

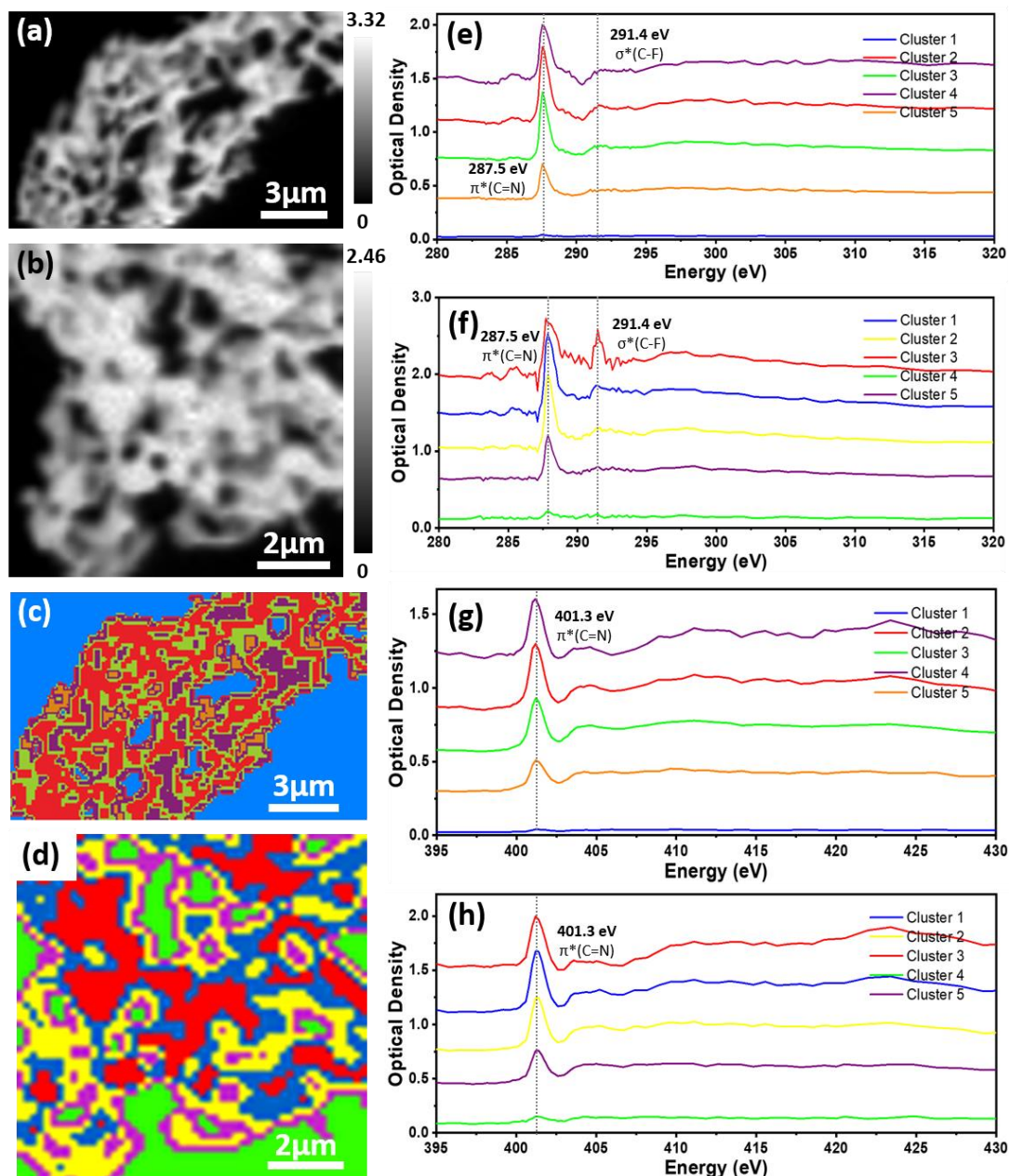


**Figure 4.** Conventional STXM results at C and N K-edge of Sn-based PVK/EMITFSI and control films. (a) Averaged STXM O.D. image from C and N K-edge of the control sample. (b) Averaged STXM O.D. image from C and N K-edge of the PVK/EMITFSI sample. (c) The PCA-CA analysis for different components of the control sample. (d) The PCA-CA analysis for different components of the PVK/EMITFSI sample. (e, f) XAS spectra at C K-edge in different regions extracted from (c) and (d), respectively. (g, h) XAS spectra at N K-edge in different regions extracted from (c) and (d), respectively.

The above observations on the STXM data of the two perovskites provide valuable clues to understand the mechanism of EMITFSI on Sn-based perovskites. The control sample without addition of EMITFSI exhibited an inhomogeneous distribution of Sn

and I, with Sn dissolution from I, which may have been caused by rapid crystallization during preparation, leading to phase inhomogeneity and numerous defects. Conversely, the PVK/EMITFSI film showed a more uniform perovskite phase, possibly due to the ionic liquid's ability to passivate defects and slow down crystallization. Based on the performance of a similar ionic liquid in Pb-based perovskites<sup>31</sup>, it is believed that the non-volatile, strongly electron-donating 1-Ethyl-3-methylimidazolium cations in the EMITFSI ionic liquid may form a protective layer around the organic components of Sn-based perovskite samples, reducing radiative charge recombination and stabilizing the perovskite phase.

## Conclusions

In this study, we utilized conventional STXM and advanced spectro-ptychography techniques to examine the impact and underlying mechanisms of EMITFSI on Sn-based perovskites. From the analysis of Sn, I  $M_{5,4}$ -edges, as well as O K-edge, we found that the Sn-based perovskite sample presents a perovskite phase with a more homogeneous chemical environment and structure after the addition of EMITFSI. This is confirmed by the STXM data of C and N K-edges, which show that the non-volatile organic cations in EMITFSI form a protective layer around the organic components of the perovskite, contributing positively to its formation and stability. The results and analysis presented above highlight the effectiveness of STXM and spectro-ptychography techniques in gaining insights into the interactions between Sn-based perovskites and additives. These techniques offer spatially resolved XANES spectra at C, N, O K-edges, and Sn, I  $M_{5,4}$ -edges, providing a comprehensive understanding of the electronic and chemical states of the various components in Sn-based perovskites. In particular, the high-resolution ptychography technique provides improved characterization of the morphology, size, and structure of perovskite nanocrystals, enabling better detection and characterization of defects and impurities in Sn-based perovskite materials from both absorption and phase aspects. Future studies aim to

utilize the combination of STXM and ptychography techniques with *in situ* heated sample holders to investigate the thermal stability effects and mechanisms of various ionic liquids and dopants on Sn-based perovskites.

## Acknowledgements

The research described in this paper was performed at the MYSTIIC of UE48\_EMIL in the BESSY II light source, Helmholtz-Zentrum Berlin für Materialien und Energie, Germany, and at Ambient STXM of SM beamline in the Canadian Light Source, the University of Saskatchewan, Canada, which is supported by the Canada Foundation for Innovation (CFI), the Natural Sciences and Engineering Research Council (NSERC), the National Research Council (NRC), the Canadian Institutes of Health Research (CIHR), the Government of Saskatchewan, and the University of Saskatchewan. We thank Helmholtz-Zentrum Berlin für Materialien und Energie and the Canadian Light Source for the allocation of synchrotron radiation beamtime. We also acknowledge Prof. Simone Raoux for her kind support and help in STXM experiments.

## Conflict of Interest:

The authors declare no conflict of interest.

## Supporting Information Available:

CHEMICAL STRUCTURE OF EMITFSI, OXYGEN K-EDGE ANALYSIS OF CONVENTIONAL STXM, and DESCRIPTION OF PCA-CA ANALYSIS

## References:

- (1) Chen, P.; Ong, W.-J.; Shi, Z.; Zhao, X.; Li, N. Pb-Based Halide Perovskites: Recent Advances in Photo(Electro)Catalytic Applications and Looking Beyond. *Adv. Funct. Mater.* **2020**, *30* (30), 1909667. <https://doi.org/10.1002/adfm.201909667>.

- (2) Su, P.; Liu, Y.; Zhang, J.; Chen, C.; Yang, B.; Zhang, C.; Zhao, X. Pb-Based Perovskite Solar Cells and the Underlying Pollution behind Clean Energy: Dynamic Leaching of Toxic Substances from Discarded Perovskite Solar Cells. *J. Phys. Chem. Lett.* **2020**, *11* (8), 2812–2817. <https://doi.org/10.1021/acs.jpcelett.0c00503>.
- (3) Ke, W.; Kanatzidis, M. G. Prospects for Low-Toxicity Lead-Free Perovskite Solar Cells. *Nat. Commun.* **2019**, *10* (1), 965. <https://doi.org/10.1038/s41467-019-08918-3>.
- (4) Li, G.; Su, Z.; Li, M.; Yang, F.; Aldamasy, M. H.; Pascual, J.; Yang, F.; Liu, H.; Zuo, W.; Di Girolamo, D.; Iqbal, Z.; Nasti, G.; Dallmann, A.; Gao, X.; Wang, Z.; Saliba, M.; Abate, A. Ionic Liquid Stabilizing High-Efficiency Tin Halide Perovskite Solar Cells. *Adv. Energy Mater.* **2021**, *11* (32), 2101539. <https://doi.org/10.1002/aenm.202101539>.
- (5) Chao, L.; Xia, Y.; Duan, X.; Wang, Y.; Ran, C.; Niu, T.; Gu, L.; Li, D.; Hu, J.; Gao, X.; Zhang, J.; Chen, Y. Direct and Stable  $\alpha$ -Phase Formation via Ionic Liquid Solvation for Formamidinium-Based Perovskite Solar Cells. *Joule* **2022**, *6* (9), 2203–2217. <https://doi.org/10.1016/j.joule.2022.07.008>.
- (6) Chao, L.; Niu, T.; Gu, H.; Yang, Y.; Wei, Q.; Xia, Y.; Hui, W.; Zuo, S.; Zhu, Z.; Pei, C.; Li, X.; Zhang, J.; Fang, J.; Xing, G.; Li, H.; Huang, X.; Gao, X.; Ran, C.; Song, L.; Fu, L.; Chen, Y.; Huang, W. Origin of High Efficiency and Long-Term Stability in Ionic Liquid Perovskite Photovoltaic. *Research* **2020**, *2020*. <https://doi.org/10.34133/2020/2616345>.
- (7) Gao, X.-X.; Ding, B.; Kanda, H.; Fei, Z.; Luo, W.; Zhang, Y.; Shibayama, N.; Züttel, A.; Tirani, F. F.; Scopelliti, R.; Kinger, S.; Zhang, B.; Feng, Y.; Dyson, P. J.; Nazeeruddin, M. K. Engineering Long-Term Stability into Perovskite Solar Cells via Application of a Multi-Functional TFSI-Based Ionic Liquid. *Cell Rep. Phys. Sci.* **2021**, *2* (7), 100475. <https://doi.org/10.1016/j.xcrp.2021.100475>.
- (8) Shen, D.; Luo, C.; Zheng, R.; Li, Q.; Chen, Y. Improvement of Photoluminescence Intensity and Film Morphology of Perovskite by Ionic Liquids Additive. *E3S Web Conf.* **2021**, *257*, 03066. <https://doi.org/10.1051/e3sconf/202125703066>.
- (9) Lee, S. J.; Shin, S. S.; Kim, Y. C.; Kim, D.; Ahn, T. K.; Noh, J. H.; Seo, J.; Seok, S. I. Fabrication of Efficient Formamidinium Tin Iodide Perovskite Solar Cells through SnF<sub>2</sub>-Pyrazine Complex. *J. Am. Chem. Soc.* **2016**, *138* (12), 3974–3977. <https://doi.org/10.1021/jacs.6b00142>.
- (10) Liu, X.; Wang, Y.; Xie, F.; Yang, X.; Han, L. Improving the Performance of Inverted Formamidinium Tin Iodide Perovskite Solar Cells by Reducing the Energy-Level Mismatch. *ACS Energy Lett.* **2018**, *3* (5), 1116–1121. <https://doi.org/10.1021/acsenergylett.8b00383>.
- (11) Liu, C.; Tu, J.; Hu, X.; Huang, Z.; Meng, X.; Yang, J.; Duan, X.; Tan, L.; Li, Z.; Chen, Y. Enhanced Hole Transportation for Inverted Tin-Based Perovskite Solar Cells with High Performance and Stability. *Adv. Funct. Mater.* **2019**, *29* (18), 1808059. <https://doi.org/10.1002/adfm.201808059>.
- (12) Shao, S.; Dong, J.; Duim, H.; ten Brink, G. H.; Blake, G. R.; Portale, G.; Loi, M. A. Enhancing the Crystallinity and Perfecting the Orientation of Formamidinium Tin Iodide for Highly Efficient Sn-Based Perovskite Solar Cells. *Nano Energy* **2019**, *60*, 810–816. <https://doi.org/10.1016/j.nanoen.2019.04.040>.
- (13) Diau, E. W.-G.; Jokar, E.; Rameez, M. Strategies To Improve Performance and Stability for Tin-Based Perovskite Solar Cells. *ACS Energy Lett.* **2019**, *4* (8), 1930–1937. <https://doi.org/10.1021/acsenergylett.9b01179>.
- (14) de Smit, E.; Swart, I.; Creemer, J. F.; Hovelings, G. H.; Gilles, M. K.; Tylliszczak, T.; Kooyman, P. J.; Zandbergen, H. W.; Morin, C.; Weckhuysen, B. M.; de Groot, F. M. F. Nanoscale Chemical

Imaging of a Working Catalyst by Scanning Transmission X-Ray Microscopy. *Nature* **2008**, 456 (7219), 222–225. <https://doi.org/10.1038/nature07516>.

(15) Witte, K.; Späth, A.; Finizio, S.; Donnelly, C.; Watts, B.; Sarafimov, B.; Odstrcil, M.; Guizar-Sicairos, M.; Holler, M.; Fink, R. H.; Raabe, J. From 2D STXM to 3D Imaging: Soft X-Ray Laminography of Thin Specimens. *Nano Lett.* **2020**, 20 (2), 1305–1314. <https://doi.org/10.1021/acs.nanolett.9b04782>.

(16) Park, J.; Kim, S.-J.; Kim, K.; Jeoun, Y.; Yu, S.-H.; Kim, C.; Sung, Y.-E.; Cairns, E. J. Understandings about Functionalized Porous Carbon via Scanning Transmission X-Ray Microscopy (STXM) for High Sulfur Utilization in Lithium-Sulfur Batteries. *Nano Energy* **2022**, 100, 107446. <https://doi.org/10.1016/j.nanoen.2022.107446>.

(17) Sun, T.; Zhang, X.; Xu, Z.; Wang, Y.; Guo, Z.; Wang, J.; Tai, R. A Bidirectional Scanning Method for Scanning Transmission X-Ray Microscopy. *J. Synchrotron Radiat.* **2021**, 28 (2), 512–517. <https://doi.org/10.1107/S1600577520016112>.

(18) Gianoncelli, A.; Bonanni, V.; Gariani, G.; Guzzi, F.; Pascolo, L.; Borghes, R.; Billè, F.; Kourousias, G. Soft X-Ray Microscopy Techniques for Medical and Biological Imaging at TwinMic—Elettra. *Appl. Sci.* **2021**, 11 (16). <https://doi.org/10.3390/app11167216>.

(19) Michelin, A.; Drouet, E.; Foy, E.; Dynes, J. J.; Neff, D.; Dillmann, P. Investigation at the Nanometre Scale on the Corrosion Mechanisms of Archaeological Ferrous Artefacts by STXM. *J Anal Spectrom* **2013**, 28 (1), 59–66. <https://doi.org/10.1039/C2JA30250K>.

(20) Leon, Y.; Saheb, M.; Drouet, E.; Neff, D.; Foy, E.; Leroy, E.; Dynes, J. J.; Dillmann, P. Interfacial Layer on Archaeological Mild Steel Corroded in Carbonated Anoxic Environments Studied with Coupled Micro and Nano Probes. *Corros. Sci.* **2014**, 88, 23–35. <https://doi.org/10.1016/j.corsci.2014.07.005>.

(21) Wang, Y.; Yang, J.; Han, H.; Hu, Y.; Wang, J.; Feng, Y.; Yu, B.; Xia, X.; Darma, A. Differential Transformation Mechanisms of Exotic Cr(VI) in Agricultural Soils with Contrasting Physio-Chemical and Biological Properties. *Chemosphere* **2021**, 279, 130546. <https://doi.org/10.1016/j.chemosphere.2021.130546>.

(22) COKER, V. S.; BYRNE, J. M.; TELLING, N. D.; VAN DER LAAN, G.; LLOYD, J. R.; HITCHCOCK, A. P.; WANG, J.; PATTRICK, R. A. D. Characterisation of the Dissimilatory Reduction of Fe(III)-Oxyhydroxide at the Microbe – Mineral Interface: The Application of STXM–XMCD. *Geobiology* **2012**, 10 (4), 347–354. <https://doi.org/10.1111/j.1472-4669.2012.00329.x>.

(23) Wu, M.; Zhang, G.; Hu, Y.; Wang, J.; Sun, T.; Regier, T.; Qiao, J.; Sun, S. Graphitic-shell Encapsulated FeNi Alloy/Nitride Nanocrystals on Biomass-derived N-doped Carbon as an Efficient Electrocatalyst for Rechargeable Zn-air Battery. *Carbon Energy* **2021**, 3 (1), 176–187. <https://doi.org/10.1002/cey2.52>.

(24) Mathurin, Jérémie; Dartois, Emmanuel; Pino, Thomas; Engrand, Cécile; Duprat, Jean; Deniset-Besseau, Ariane; Borondics, Ferenc; Sandt, Christophe; Dazzi, Alexandre. Nanometre-Scale Infrared Chemical Imaging of Organic Matter in Ultra-Carbonaceous Antarctic Micrometeorites (UCAMMs). *A&A* **2019**, 622, A160. <https://doi.org/10.1051/0004-6361/201833957>.

(25) Jun, H.; Lee, H. R.; Tondelier, D.; Geffroy, B.; Schulz, P.; Bourée, J.-É.; Bonnassieux, Y.; Swaraj, S. Soft X-Ray Characterization of Halide Perovskite Film by Scanning Transmission X-Ray Microscopy. *Sci. Rep.* **2022**, 12 (1), 4520. <https://doi.org/10.1038/s41598-022-08256-3>.

(26) Dindault, C.; Jun, H.; Tondelier, D.; Geffroy, B.; Bourée, J.-E.; Bonnassieux, Y.; Schulz, P.; Swaraj, S. Metal Halide Perovskite Layers Studied by Scanning Transmission X-Ray Microscopy.

- RSC Adv.* **2022**, *12* (39), 25570–25577. <https://doi.org/10.1039/D2RA04438B>.
- (27) Sun, T.; Sun, G.; Yu, F.; Mao, Y.; Tai, R.; Zhang, X.; Shao, G.; Wang, Z.; Wang, J.; Zhou, J. Soft X-Ray Ptychography Chemical Imaging of Degradation in a Composite Surface-Reconstructed Li-Rich Cathode. *ACS Nano* **2021**, *15* (1), 1475–1485. <https://doi.org/10.1021/acsnano.0c08891>.
- (28) Sharma, V.; Vyas, R.; Bazylewski, P.; Chang, G. S.; Asokan, K.; Sachdev, K. Probing the Highly Transparent and Conducting SnO<sub>x</sub>/Au/SnO<sub>x</sub> Structure for Futuristic TCO Applications. *RSC Adv.* **2016**, *6* (35), 29135–29141. <https://doi.org/10.1039/C5RA24422F>.
- (29) Minohara, M.; Kikuchi, N.; Yoshida, Y.; Kumigashira, H.; Aiura, Y. Improvement of the Hole Mobility of SnO Epitaxial Films Grown by Pulsed Laser Deposition. *J Mater Chem C* **2019**, *7* (21), 6332–6336. <https://doi.org/10.1039/C9TC01297D>.
- (30) Zhu, X.; Hitchcock, A. P.; Bazylinski, D. A.; Denes, P.; Joseph, J.; Lins, U.; Marchesini, S.; Shiu, H.-W.; Tyliczszak, T.; Shapiro, D. A. Measuring Spectroscopy and Magnetism of Extracted and Intracellular Magnetosomes Using Soft X-Ray Ptychography. *Proc. Natl. Acad. Sci.* **2016**, *113* (51). <https://doi.org/10.1073/pnas.1610260114>.
- (31) Wang, S.; Guo, H.; Wu, J.; Lei, Y.; Li, X.; Fang, Y.; Dai, Y.; Xiang, W.; Lin, Y. High-Conductivity Thiocyanate Ionic Liquid Interface Engineering for Efficient and Stable Perovskite Solar Cells. *Chem. Commun.* **2022**, *58* (60), 8384–8387. <https://doi.org/10.1039/D2CC02354G>.